Supporting information for: Rectification of Current Responds to Incorporation of Fullerenes into Mixed-Monolayers of Alkanethiolates in Tunneling Junctions

Li Qiu, Yanxi Zhang, Theodorus L. Krijger, Xinkai Qiu, Patrick van 't Hof, Jan C. Hummelen, and Ryan C. Chiechi*

Stratingh Institute for Chemistry & Zernike Institute for Advanced Materials, University of Groningen, Nijenborgh 4, 9747 AG Groningen, The Netherlands

E-mail: r.c.chiechi@rug.nl

Contents

1 Experimental details

1.1 General

General: Chemicals including 11-bromoundec-1-ene, 4-hydroxybenzaldehyde, thioacetic acid, 1-decanethiol (**SC10**) were obtained from Sigma-Aldrich and used as received with the exception of **SC10** which was purified by column chromatography (silica, hexane). The C_{60} used for the syntheses was 99.5 % (purchased from Solenne BV, Groningen, The Netherlands). All compounds were stored in nitrogen-flushed vials and in the dark. The Au substrates used in this work are made by mechanic Template Stripping (mTS) described in detail elsewhere.[S1] In our case, we deposited 200 nm of Ag and 100 nm of Au (99.99%), respectively, by thermal vacuum deposition onto a 3″ Silicon wafer (with no-adhesion layer).

Using UV-curable Optical Adhesive (OA) Norland 61, we glued $1\,cm^2$ glass chips on the metal surfaces. The mTS procedure provides ultra flat smooth surfaces, which allows self-assembly process to achieve higher yields of working junctions.

Analytical TLC was performed on Merck silica gel 60/kieselguhr F254 and visualization was accomplished by UV light. Column chromatography was performed using silica gel (SiliaFlash P60 Type R12030B, 230-400 mesh). ^{1}H-NMR and ^{13}C-NMR were performed on a Varian Unity Plus (400 MHz) instrument at $25\,°C$, using tetramethylsilane (TMS) as an internal standard. NMR shifts are reported in ppm, relative to the residual protonated solvent signals of $CDCl_3$ (δ = 7.26 ppm) or at the carbon absorption in $CDCl_3$ (δ = 77.0 ppm), and multiplicities are denoted as: s = singlet, d = doublet, t = triplet and m = multiplet. IR measurements were performed on a Nicolet iS50 FT-IR spectrometer. UV-vis absorption spectra were measured with a Jenway 6715 spectrophotometer. High Resolution Mass Spectroscopy (HRMS) was performed on a JEOL JMS 600 spectrometer. Contact Angles (CA) were measured under ambient conditions on a SCA20 Dataphysics instrument with software version 3.60.2. Equilibrium contact angles were obtained by applying 1 µL water droplets on SAMs using the sessile drop method. The contact angle was measured at three different locations on each surface and the results were averaged. XPS measurements were performed using a *VG Microtech* spectrometer with a hemispherical electron analyzer, and a Mg Kα (1253.6 eV) X-ray source. CP-AFM *I-V* measurements were performed on a Bruker AFM Multimode MMAFM-2 equipped with a Peak Force TUNA Application Module (Bruker). The SAMs were contacted with an Au-coated silicon nitride tip with a nominal radius of 30 nm (NPG-10, Bruker, tip A: resonant frequency 65 kHz, spring constant: 0.35 N/m; tip B: resonant frequency: 23 kHz, spring constant: 0.12 N/m; tip D: resonant frequency: 18 kHz, spring constant: 0.06 N/m) in TUNA mode with loading force of 1.4 nN (tip A), 0.48 nN (tip B) and 0.24 nN (tip D), respectively. The AFM tip was grounded and for loading force of 1.4 nN, the sample was biased from -1.5 V to +1.5 V and from +1.5 V

to -1.5 V (while for loading force of 0.48 nN and 0.24 nN, the sample was biased from -2 V to +2 V and from +2 V to -2 V) to record the I-V curve (512 points per trace were taken): a max of 30 trace/re-trace cycles per junction were performed. After every junction, the tip was withdrawn and moved to a different spot, and engaged again for a total of 39 (for 1.4 nN of loading force), 20 (for 0.48 nN of loading force) and 10 (for 0.24 nN of loading force) junctions per sample analyzed. Between different samples a new tip was used. The data were analyzed with the same software used for EGaIn using the current I instead of the current density J. The obtained $\log|I|(V)$ plots and $\log|R|(V)$ are shown in Figure S6.

1.2 Synthesis

The synthesis of compound **FSC11** is straightforward, as shown in Scheme S1. By treating the commercially available 4-hydroxybenzaldehyde with 11-bromo-1-undecene under basic conditions, 4-(10-Undecenyloxy)benzaldehyde could be obtained in good yield, which was then converted to the thioester 4-(11-thioacetoxyundecyl)benzaldehyde through a free radical-mediated nucleophilic addition(azo-bis-isobutyronitrile (AIBN) as the radical initiator). The Prato reaction[S2] then gave the corresponding **FSC11-Ac**, which experienced dibutyltin oxide-mediated transesterification with methanol to give the target C60-thiol **FSC11**.[S3] New compounds were all fully characterized by means of HRMS, NMR and IR.

4-(10-Undecenyloxy)benzaldehyde. The procedure for the synthesis of this compound was taken from the literature.[S4] 11-Bromo-1-undecene (4.38 mL, 4.66 g, 20 mmol), 4-hydroxybenzaldehyde (2.44g, 20 mmol), tetrabutylammonium iodide (catalytic amount, 0.20 g) and potassium carbonate (13.80 g, 100 mmol) were introduced into acetone (100 mL). After refluxing for 6 h, the mixture was allowed to cool to room temperature and the solids were filtered off. The filtrate was concentrated in vacuo and the crude product was purified by column chromatography (ethyl acetate:hexane = 1:9) to give 5g product as a colorless oil

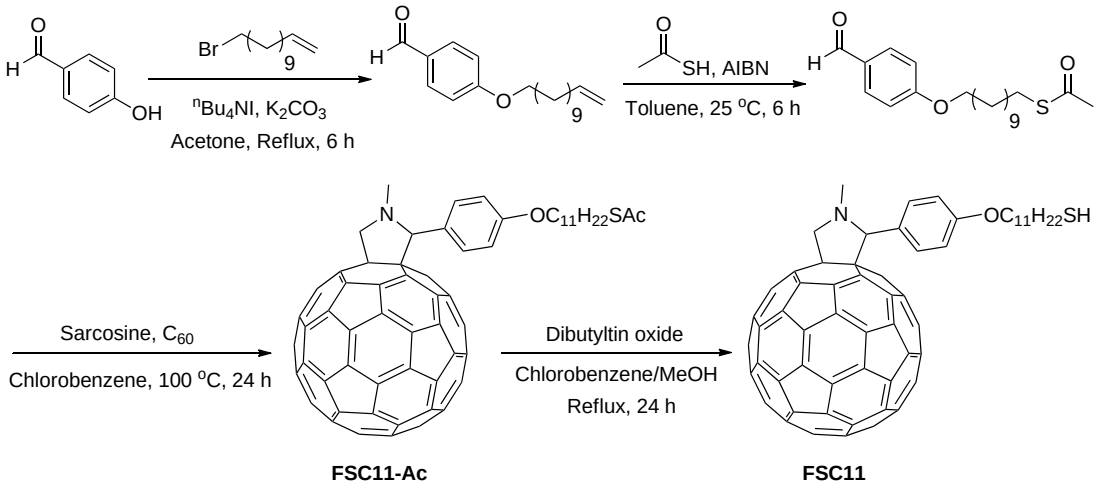

Figure S1: Synthetic route of **FSC11**

(90%).

4-(11-Thioacetoxyundecyl)benzaldehyde. The procedure for the synthesis of this compound was taken but lightly improved from the literature.[S5] 4-(10-Undecenyloxy)benzaldehyde (2.74 g; 10 mmol), thioacetic acid (7.13 mL; 100 mmol), and azo-bis-isobutyronitrile (AIBN, 30 mg; 0.18 mmol) were dissolved in 40 mL of toluene. The mixture was degassed with a stream of N_2 and then stirred at room temperature for 8 h. The reaction was quenched with 5% aqueous $NaHCO_3$ and extracted three times with ethyl acetate. The combined organic layers were washed with 5% aqueous $NaHCO_3$ and then brine and dried over $MgSO_4$. Upon filtration and removal of the solvent under reduced pressure, the yellow solid residue was then purified by column chromatography on silica eluting with a gradient of pure toluene to pure chloroform. The crude product obtained was recrystallized from methanol to afford 1.41 g (42%) of the title aldehyde as a white powder.

FSC11-Ac. An oven-dried three-necked, 500 mL round-bottom flask was charged with C_{60}

(1.44 g, 2 mmol), 4-(11-thioacetoxyundecyl)benzaldehyde (700 mg, 2 mmol), sarcosine (720 mg, 8 mmol) and chlorobenzene (200 mL). The reaction mixture was stirred under N_2 at 100 °*C* for 24 h. The mixture was concentrated in vacuo to 15 mL, and the crude residue was purified by column chromatography (Silica gel; CS_2 followed by toluene) to afford the pure compound as a brown solid. The product was redissolved in 7 mL of chlorobenzene, precipitated with MeOH, washed repeatedly with MeOH and pentane, and dried in vacuo at 50 °*C*. This procedure gave 600 mg (0.55 mmol, 27%) of **FSC11-Ac**.

^{1}H-NMR (400 MHz, CS_2 / D_2O) δ 7.84 (s, 2H), 7.05 (d, J = 8.1 Hz, 2H), 5.16 (d, J = 9.2 Hz, 1H), 5.07 (s, 1H), 4.46 (d, J = 9.2 Hz, 1H), 4.11 (t, J = 6.3 Hz, 2H), 3.01 (s, 3H), 2.48 (s, 3H), 2.06 1.92 (m, 2H), 1.80 1.64 (m, 4H), 1.52 (s, 14H). ^{13}C-NMR (100 MHz, CS_2 / D_2O) δ 162.1, 159.1, 156.8, 156.4, 156.3, 150.0, 149.6, 149.3, 149.2, 149.1, 149.0, 148.9, 148.7, 148.6, 148.5, 148.3, 148.2, 148.1, 148.0, 147.5, 147.2, 146.0, 145.9, 145.5, 145.4, 145.1, 145.0, 144.9, 144.8, 144.7, 144.5, 144.4, 143.1, 143.0, 142.8, 142.5, 139.6, 139.5, 138.6, 133.1, 131.2, 117.5, 86.0, 80.2, 72.9, 71.7, 70.6, 42.9, 33.1, 33.0, 32.9, 32.8, 32.7, 32.5, 32.3, 32.2, 29.5. IR (cm^{-1}): 2923, 2849, 2777, 2326, 1687, 1609, 1506, 1461, 1330, 1243, 1171, 1105, 1029, 946, 831, 702. HRMS(ESI) calcd. for $C_{82}H_{36}NO_2S[M+H]^+$: 1098.24613, found: 1098.24992.

FSC11. The solution of **FSC11-Ac** (300 mg, 0.27mmol) and dibutyltin oxide (3.42mg, 0.014mmol, 5mol%) in chlorobenzene (60 ml) and methanol (30 ml) was heated to reflux for 24 h under N_2. The mixture was concentrated in vacuo to 15 mL, and the crude residue was purified by column chromatography (Silica gel; toluene/hexane=1/1 followed by toluene) to afford the pure compound as a brown solid. The product was redissolved in 7 mL of chlorobenzene, precipitated with MeOH, washed repeatedly with MeOH and pentane, and dried in vacuo at 50 °*C*. This procedure gave 88 mg (0.55 mmol, 30%) of **FSC11**.

^{1}H-NMR (400 MHz, $CDCl_3$) δ 7.69 (s, 2H), 6.94 (d, J = 8.2 Hz, 2H), 4.97 (d, J = 8.7 Hz, 1H), 4.88 (s, 1H), 4.24 (d, J = 9.1 Hz, 1H), 3.95 (t, J = 6.5 Hz, 2H), 2.79 (s, 3H), 2.51 (dd, J = 14.7, 7.4 Hz, 2H), 1.83 1.71 (m, 2H), 1.68 1.52 (m, 3H), 1.50 1.21 (m, 14H). ^{13}C-NMR

(100 MHz, $CDCl_3$) δ 161.9, 159.0, 156.8, 156.3, 150.0, 149.9, 149.5, 149.2, 149.0, 148.9, 148.8, 148.7, 148.6, 148.4, 148.2, 148.1, 148.0, 147.9, 147.8, 147.4, 147.3, 147.0, 145.8, 145.6, 145.3, 145.2, 144.9, 144.8, 144.7, 144.6, 144.5, 144.3, 144.2, 142.8, 142.6, 142.2, 139.5, 139.3, 138.4, 133.1, 131.3, 117.2, 85.9, 72.6, 71.6, 70.6, 42.7, 36.7, 32.2, 32.1, 32.0, 31.7, 31.0, 28.7, 27.3. IR (cm^{-1}): 2918, 2848, 2773, 1604, 1510, 1461, 1424, 1330, 1243, 1168, 1103, 1025, 908, 829, 702. HRMS(ESI) calcd. for $C_{80}H_{34}NOS[M+H]^+$: 1056.23556, found: 1056.23989.

2 Electrical Measurements

2.1 Histogram of $\log|R|$ and current density

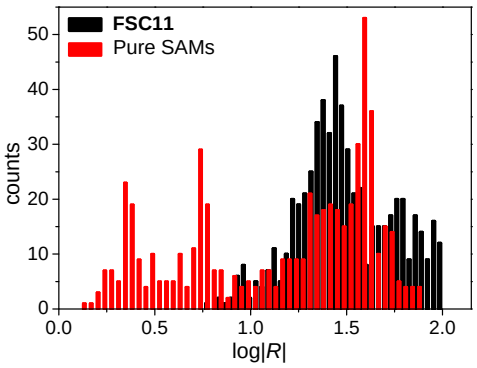

Figure S2: Histograms of $\log|R|$ for pure SAMs and **FSC11** on Ag^{TS} obtained by dividing each value of J at positive bias into the corresponding value at negative bias for every value of $|V|$ for 567 and 650 J/V traces, respectively. While $\log|R|$ for **FSC11** SAMs (mixed monolayers) produced a single Gaussian centered near 1.5, the data of the pure SAMs are distributed from $0-2$ and likely comprise multiple peaks. We interpret this difference to competition from the strong fullerene-fullerene and fullerene-Ag interactions (discussed in the main text) that preclude the formation of a well-ordered SAM.

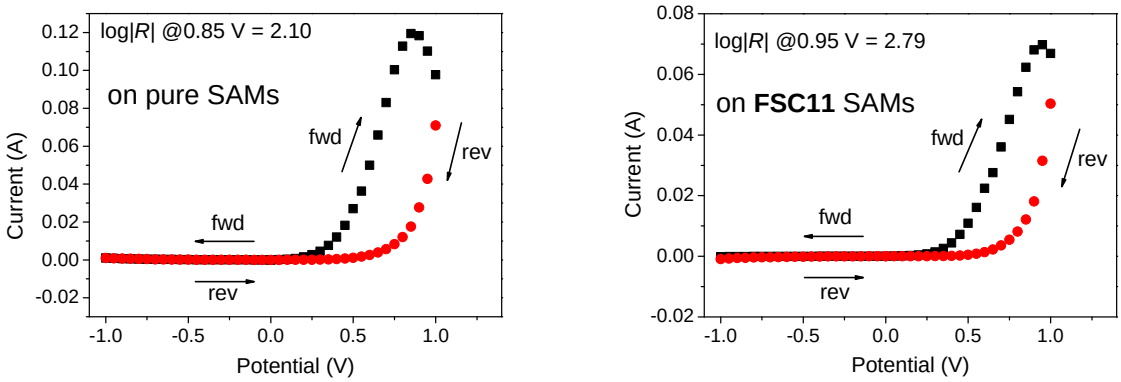

Figure S3: I/V data for representative junctions that produce stable I/V curves above 0.5 V showing typical degrees of hysteresis based both on pure **FSC11** SAMs (left) and on mixed **FSC11** SAMs (right) on Ag^{TS}.

2.2 Plots of $\log|R|$, $\log|J|$ and $\log|I|$ *versus* V

3 Characterization

3.1 Contact angle measurement

The SAM of **FSC11** was evaluated with water contact angle measurements, before the exchanging, the SAM of **SC10** (left) was determined to be more hydrophobic and showed an average contact angle of 94 ± 1°, while after exchanging, the fullerene SAM of **FSC11** was formed with an average contact angle of 68 ± 1°, which is corresponding closely to values of C_{60}-SAM reported by Tsukruk and co-workers.[S6]

3.2 XPS thickness measurement

To measure the thickness of the SAM we acquire the $Ag_{3p3/2}$ and Ag_{3d} peaks with the sample rotated under 0, 10, 20, 30, 40, and 50 degrees. A Gaussian fit with background is made to the peaks to obtain their intensities. To correct for slow fluctuations in the X-ray source intensity we acquire a spectrum for each peak at 0 degrees in between the measurements where the sample is rotated. These measurements are used to obtain a correction factor γ_I.

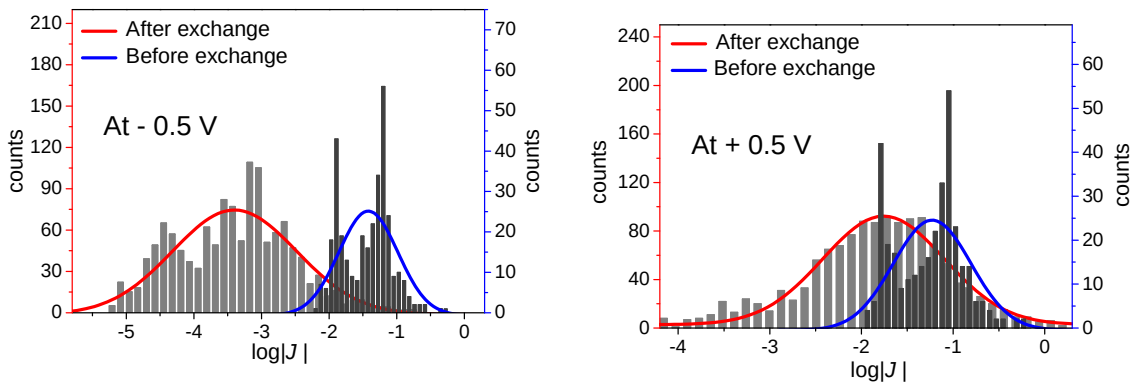

Figure S4: Histograms of current density of **FSC11** and **SC10** at - 0.5 V (left) and + 0.5 V (right) in the Ag^{TS}/**FSC11** or **SC10**//Ga_2O_3/EGaIn junctions. The maximum value of $\log|J|$ at $-0.5\,V$ drops below -3, while the value at $0.5\,V$ remains almost equal to that of **SC10**. The suppression of leakage current (at negative bias) compared to the SAM of pure **SC10** is caused by the increase in tunneling distance imposed by the fullerene group. At positive bias, the LUPS is sufficiently close to E_f of Ag electrode that charges can be mediated by LUPS of C_{60} cage and tunneling occurs only through the aliphatic portion of the SAM (followed by hopping between C_{60} cage and EGaIn), leading to a nearly equal magnitude of J for SAMs of **SC10** and **FSC11** at $0.5\,V$. This asymmetry results in an obvious current rectification.

This factor was used to normalize the peak intensities to acquire $I^* = \gamma_I I$, which was used to fit the thickness of the layer. The values are given in Table S1.

Table S1: measured XPS peak intensities (I), correction factor γ_I, and the corrected peak intensities (I^*) for the Ag3d and Ag3p peaks.

sample	Ag_3d			$Ag_3p_{3/2}$		
rotation (°)	I	γ_I	I^*	I	γ_I	I^*
0	8358	1.00	8358	3775	1.00	3775
10	7945	1.01	8044	2972	0.91	2715
20	7349	1.00	7333	3663	0.95	3471
30	6479	0.96	6230	3029	0.93	2820
40	5050	0.94	4748	1732	0.88	1522
50	3086	0.93	2880	1121	0.86	965

We measure the intensity of the peaks of electrons that make it from the silver through the SAM, without scattering. The intensity therefore depends on the length of the path through the overlayer, and the inelastic mean free path of the electrons. The intensity at a

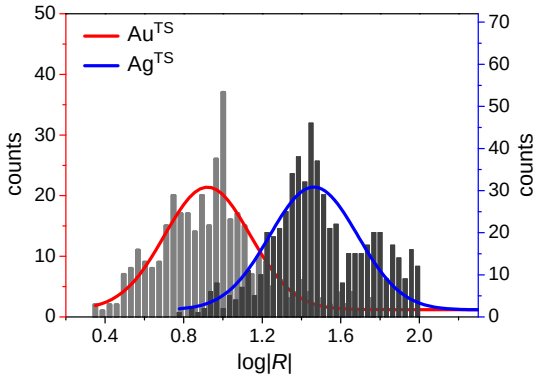

Figure S5: Histograms of $\log|R|$ for **FSC11** on Ag^{TS} and Au^{TS} obtained by dividing each value of J at positive bias into the corresponding value at negative bias for every value of $|V|$ for 650 and 366 J/V traces, respectively. The blue and red lines are Gaussian fits with peaks and standard deviations of 1.46±0.018 and 0.92±0.017 for Ag^{TS} and Au^{TS} respectively.

given angle can be expressed as:

$$I^*(\phi) = I_0 \exp(\frac{-L}{\lambda}) = I_0 \exp(\frac{-d}{\lambda \cos(\phi)})$$
$$\ln(I^*) = \ln(I_0) - \frac{d}{\lambda}\frac{1}{\cos(\phi)} \tag{S1}$$

with L the length of the path through the layer, d the thickness of the layer, λ the inelastic mean free path, and ϕ the angle of rotation of the sample with respect to the analyzer. λ depends on the kinetic energy of the observed electrons and the material the electrons have to move through. We have determined the values of λ, for electrons originating from the Ag_{3d} and Ag_{3p} levels, from measurements on a SAM of **SC10** on silver, whose thickness was well studied ((12 ± 3) Å).[S7] The values were found to be $8\,Å^{-1}$ and $8.8\,Å^{-1}$ for Ag_{3d} and Ag_{3p} respectively. With these values of λ we can make a fit to the corrected intensities to find the thickness of the **FSC11** SAM, which was found to be $d = 1.8 \pm 0.3$ nm. This treatment assumes the inelastic mean free path in the **FSC11** SAM to be equal to that in the **SC10** SAM. The lower packing density of **FSC11** could lead to a slight underestimation of the thickness of the layer.

3.3 Estimation of LUPS of FSC11

LUPS energy of **FSC11** was determined using a combination of optical and photoelectron spectroscopy. The UV-vis absorption spectrum (Figure S14) of **FSC11**, which enables the estimation of HOMO-LUMO gap (E_g). Inset shows the determination of onset wavelength to be 718.13 nm, from which E_g is extrapolated to be 1.73 eV.

Ultraviolet photoelectron spectroscopy (UPS, Figure S15) analysis of the SAM bound to Ag^{TS} is used to find the Fermi level of the silver, and the HOPS level of the **FSC11** relative to the Fermi level. Binding energies are calculated with respect to the vacuum level. The vacuum level is found by summing the secondary electron cutoff and the photon energy (He I, hν =21.2 eV). In Figure S15 the valence band spectrum is shown as measured by UPS, showing the characteristic double peak of HOMO and HOMO-1 of C_{60}. For this data a smooth background function has been subtracted. A multiple Gaussian peak fit is performed on the data and the width (σ) and center (μ) of the peaks are found from the fit. We take the value of $\mu + 2\sigma$ as the onset of the HOMO, which is found to be -5.45 eV. From the equation $E_{LUMO} = E_{HOMO} + E_g$ (eV), E_{LUMO} is extropolated to be -3.72 eV.

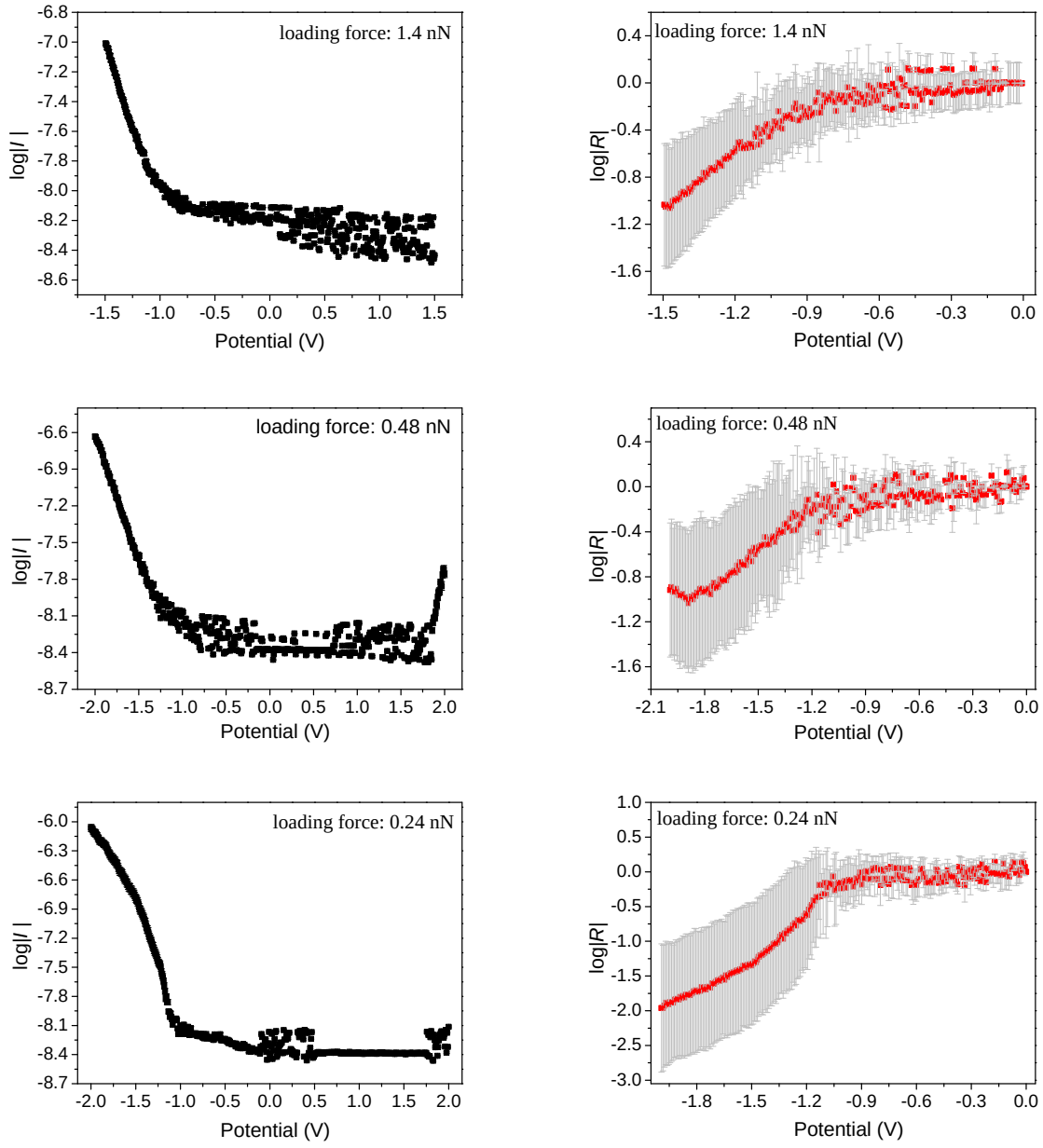

Figure S6: Plots of $\log|I|$ (left) $\log|R|$ (right) *versus* V of **FSC11** SAM for CP-AFM measurements at different loading forces of 1.4 nN (up) 0.48 nN (middle) and 0.24 nN (down) (the units of I are mA). CP-AFM measurements employing a rigid Au electrode instead of a conformal, liquid-metal electrode (EGaIn) shows an obvious rectification with $\log|R|$ greater than 1, meaning that the origin of rectification for the Ag^{TS}/**FSC11**//Ga_2O_3/EGaIn junction is the SAM and not Ag^{TS} or EGaIn. The error bars are standard deviations.

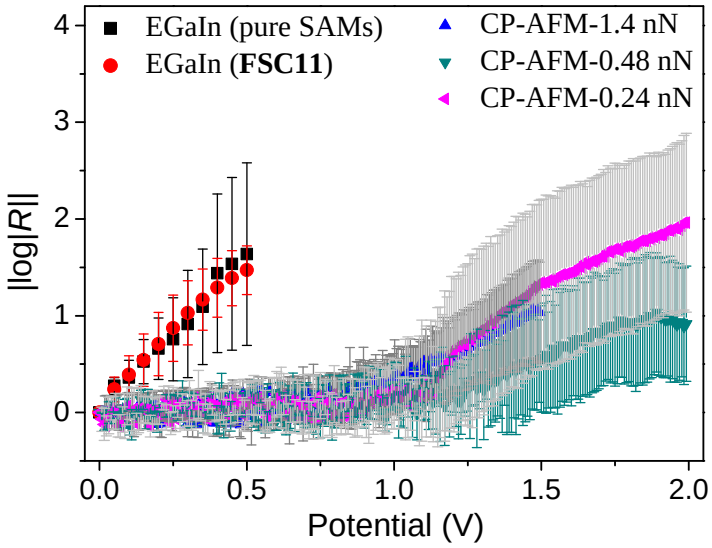

Figure S7: Comparison of $\log|R|$ vs. $|V|$ plots of EGaIn (black squares and red dots) and CP-AFM (blue, green and magenta symbols) measurements. Each data point is the peak of a Gaussian fit to a histogram of $\log|R|$ at that value of $|V|$. The error bars are the standard deviations of those fits. This same plot is shown without error bars in the Main Text for clarity.

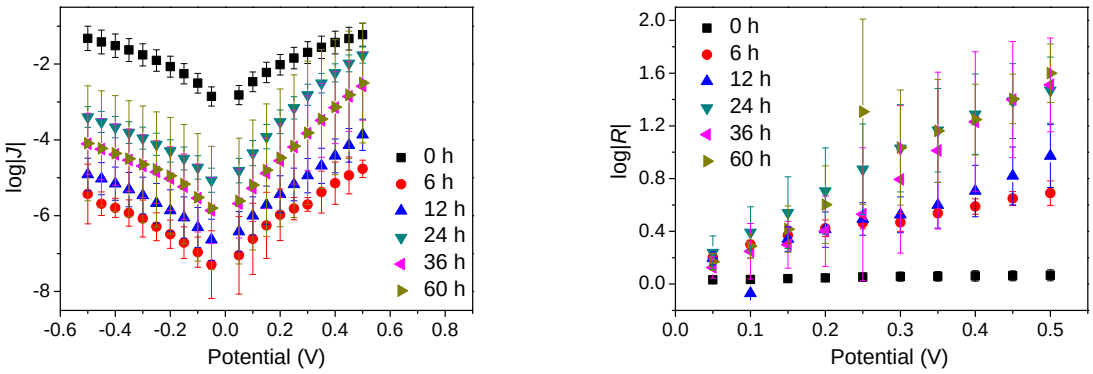

Figure S8: Plots of $\log|J|$ (left) and $\log|R|$ (right) *versus* the exchange time for the preparation of **FSC11** SAM. The magnitude of $\log|R|$ increased gradually with the exchange time below 24 h, while remained almost unchanged since then, indicating the nearly complete **FSC11** SAM was achieved after 24 h later (we did not perform the measurement for longer than 60 h because the optical adhesive began to swell).

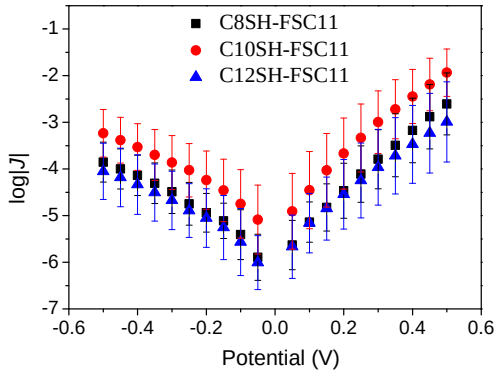

Figure S9: Plots of $\log|J|$ (left) *versus* the magnitude of applied bias after 24 h exchange for **FSC11** SAM preparation using different passivating thiols with different length of alkane chain. The magnitudes of $\log|J|$ are not significantly, which again supporting the mechanism proposed in the manuscript.

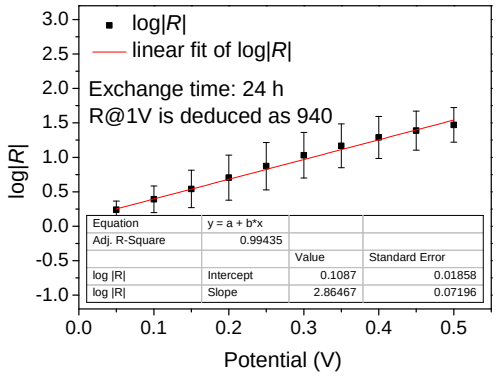

Figure S10: A plot and linear fitting of $\log|R|$ *versus* the magnitude of applied bias after 24 h exchange for **FSC11** SAM preparation. The linear dependence of $\log|R|$ on $|V|$ enables the extrapolation of the value of R at any specific $|V|$, *e.g.*, ± 0.95 V. Comparing deduced value of $R = 676$ at ± 0.95 V to $R = 617$ from a single 'hero junction' that survived sweeping to ± 0.95 V offered a close agreement.

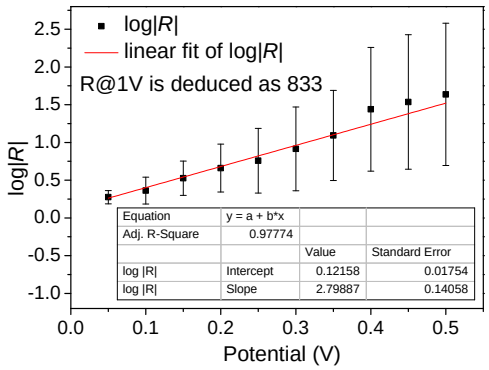

Figure S11: A plot and linear fitting of $\log|R|$ *versus* the magnitude of applied bias for pure SAMs. The linear dependence of $\log|R|$ on $|V|$ gave almost the same slope and similar deduced value of R (833) at $\pm 1.0\,\mathrm{V}$.

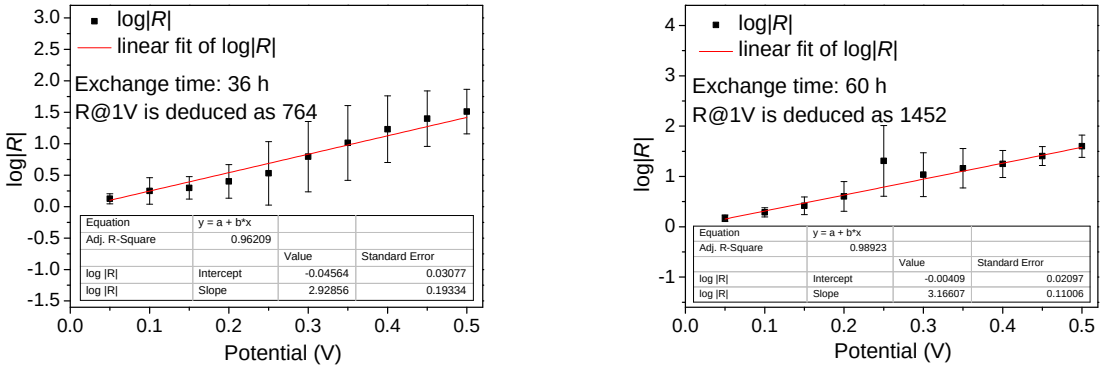

Figure S12: Plots and linear fits of $\log|R|$ *versus* the magnitude of applied bias after 36 h and 60 h exchange for **FSC11** SAM preparation. The plots of $\log|R|$ *versus* $|V|$ for SAMs of **FSC11** at different exchange times (*i.e.*, 36 h and 60 h) gave almost the same slope and similar deduced value of R at $\pm 1.0\,\mathrm{V}$, validating the extrapolated value of $|R|_{\mathrm{obsd}} = 940$ employed in the main text.

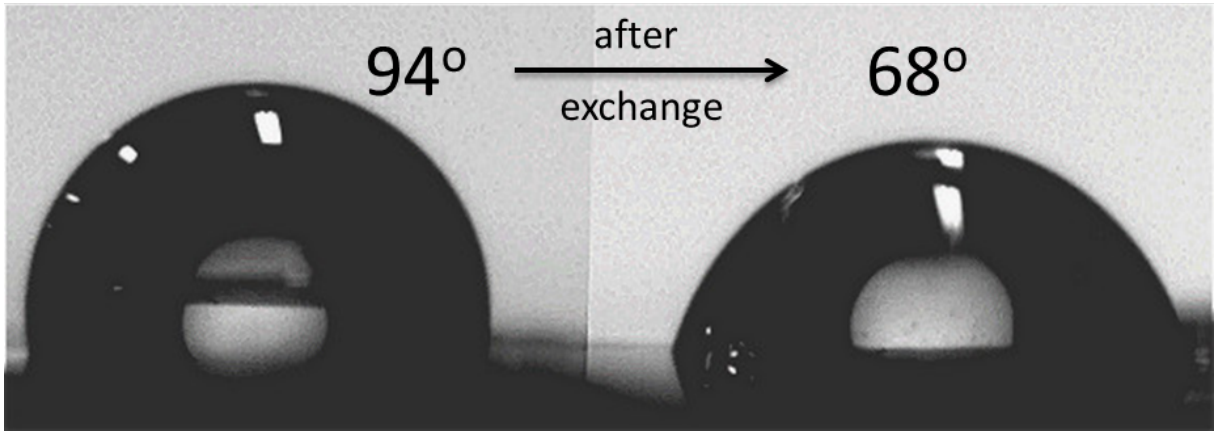

Figure S13: profiles of water contact angle of **SC10** SAM (left, before exchange) and **FSC11** SAM (right, after exchange).

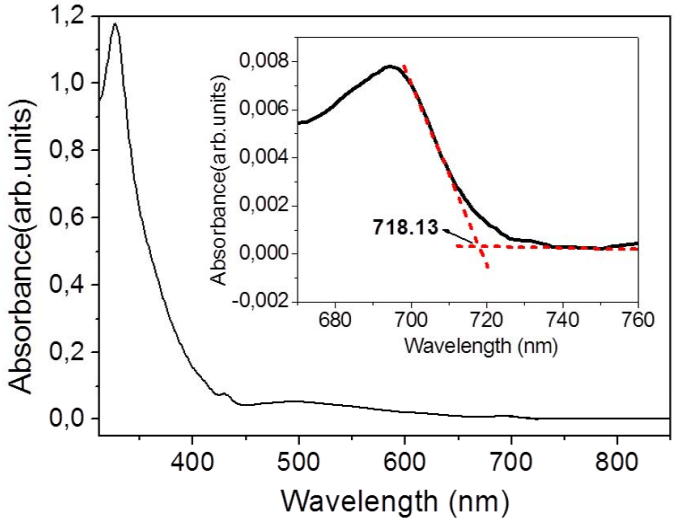

Figure S14: UV-vis absorption spectrum of **FSC11**, which enabled the estimation of HOMO-LUMO gap (E_{f}). Inset shows the determination of onset wavelength to be 718.13 nm, from which $E_{\mathrm{f}}$is extrapolated to be 1.73 eV.

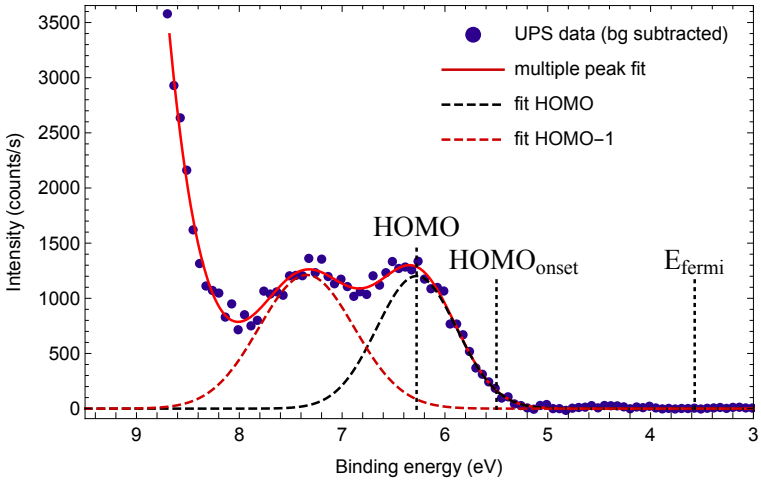

Figure S15: UPS of the **FSC11** SAM, relevant energy levels are determined to be: Vacuum level: 0 eV; Fermi level: -3.57 eV; HOMO onset: -5.45 eV.

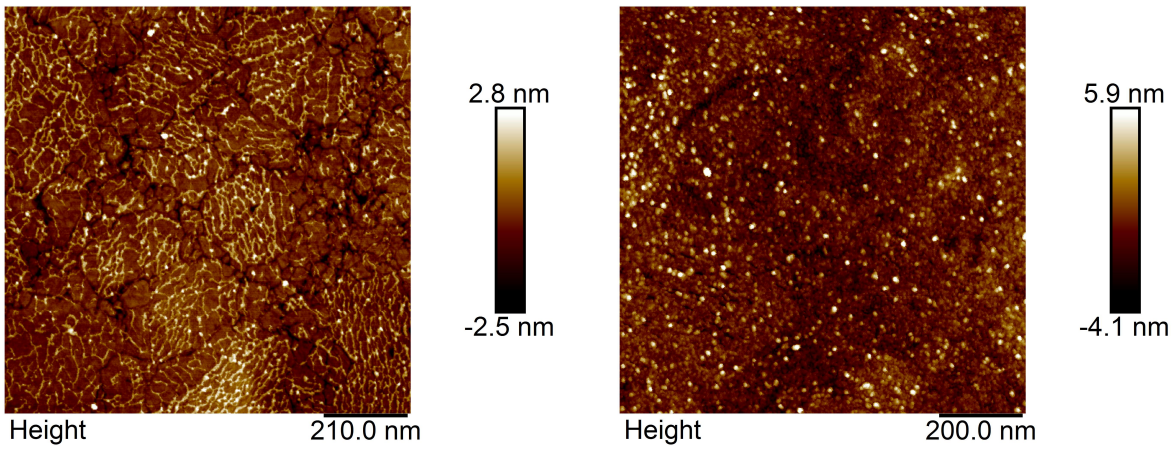

Figure S16: AFM height profiles of (left) the pure alkanethiol SAM (that is before exchange) and (right) **FSC11** SAM (after exchange, the surface of which is comparable to that in the paper.[S8] Both films looks like relatively smooth (Ra $\approx 1nm$). Although the difference before and after exchange is obvious, One could hardly draw definitive conclusions about the distribution of fullerenes since, in our hands, AFM is only barely capable of resolving 15 nm-wide protein complexes[S9] and C60 is nominally 1 nm in diameter. There are qualitative differences before and after exchange, certainly, and there are randomly-distributed spheroids in the post-exchange AFM, which could not be overinterpreted thus far.

3.4 NMR spectra

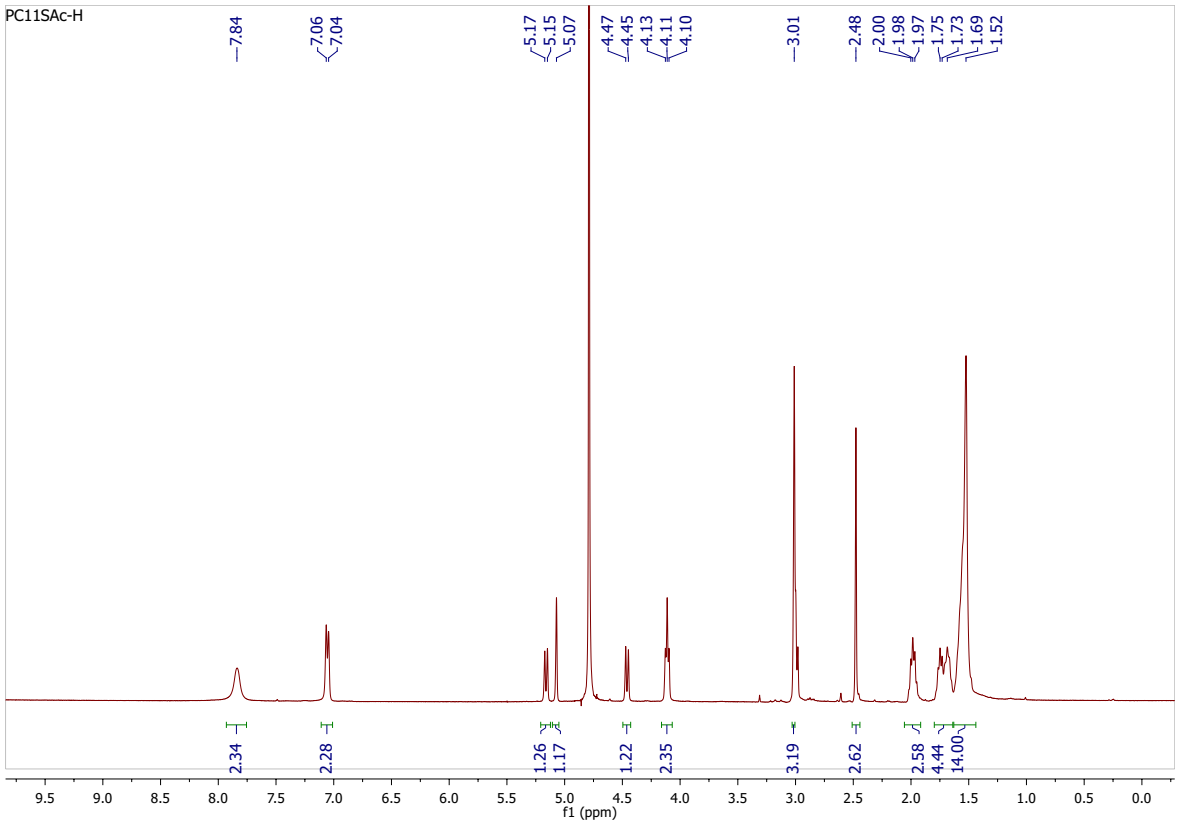

Figure S17: ^{1}H NMR spectrum of **FSC11-Ac**

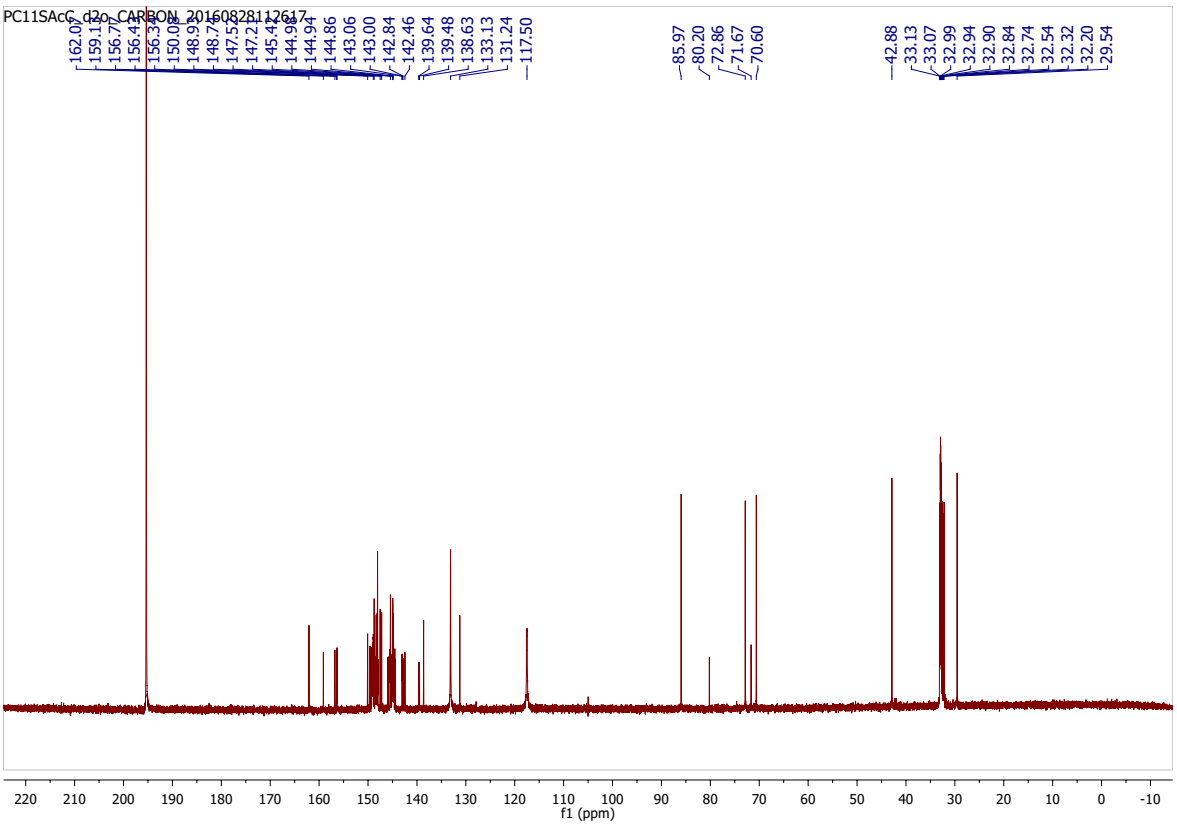

Figure S18: ^{13}C NMR spectrum of **FSC11**

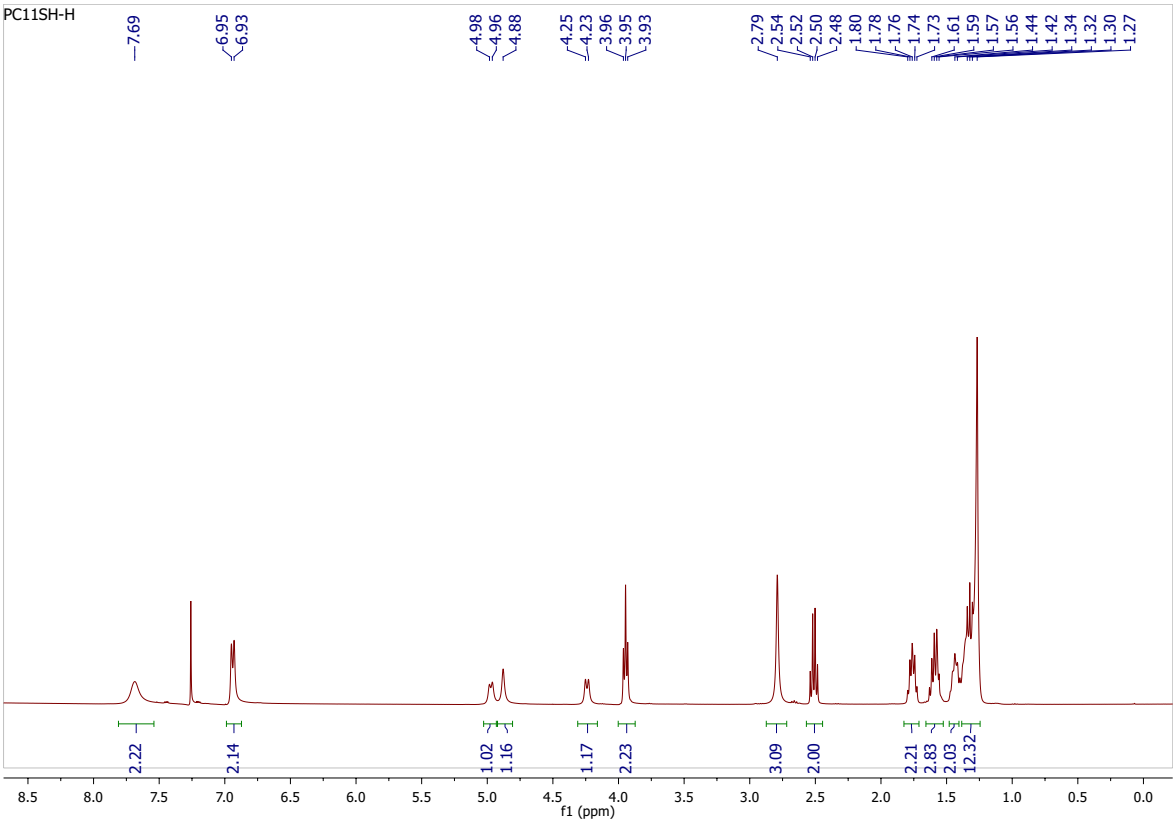

Figure S19: ^{1}H NMR spectrum of **FSC11**

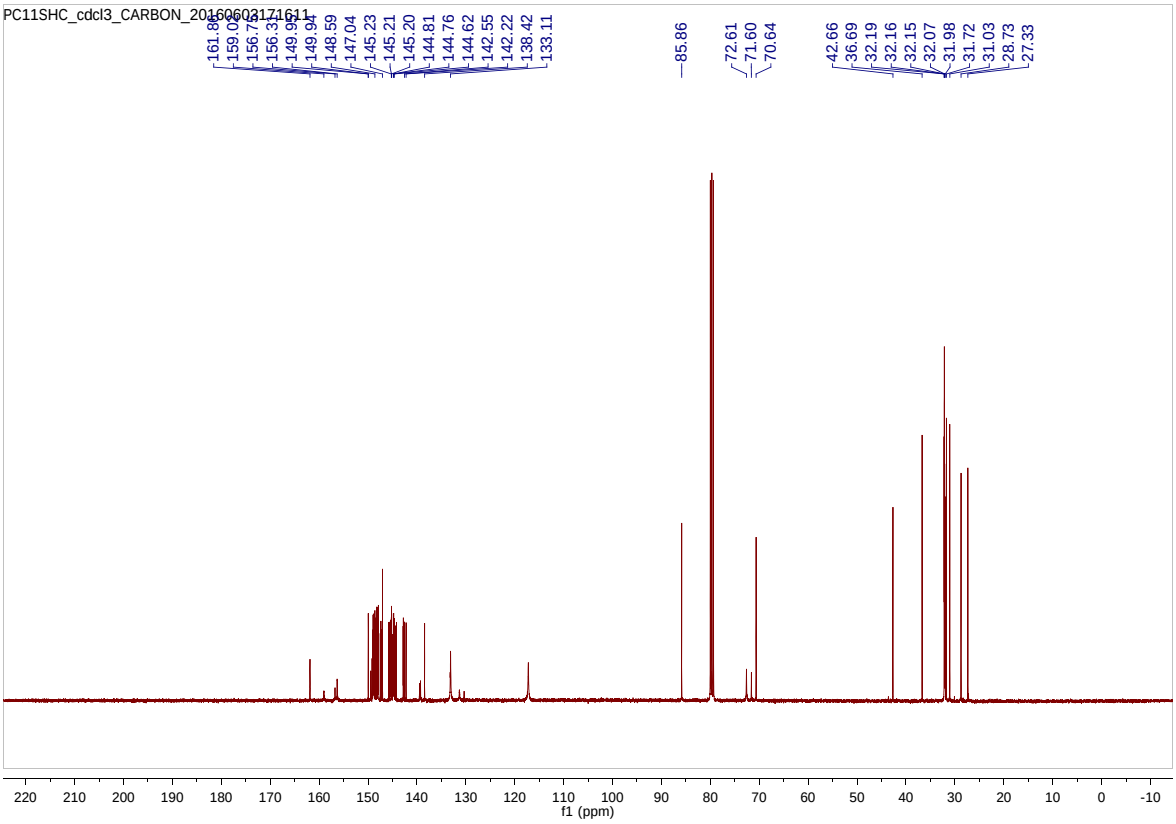

Figure S20: ^{13}C NMR spectrum of **FSC11**

References

(S1) Weiss, E. A.; Kaufman, G. K.; Kriebel, J. K.; Li, Z.; Schalek, R.; Whitesides, G. M. Si/SiO_2-templated Formation of Ultraflat Metal Surfaces on Glass, Polymer, and Solder Supports: Their Use as Substrates for Self-Assembled Monolayers. *Langmuir* **2007**, *23*, 9686–9694.

(S2) Maggini, M.; Scorrano, G.; Prato, M. Addition of Azomethine Ylides to C_{60}: Synthesis, Characterization, and Functionalization of Fullerene Pyrrolidines. *J. Am. Chem. Soc.* **1993**, *115*, 9798–9799.

(S3) Baumhof, P.; Mazitschek, R.; Giannis, A. A Mild and Effective Method for the Transesterification of Carboxylic Acid Esters. *Angew. Chem., Int. Ed.* **2001**, *40*, 3672–3674.

(S4) Lee, G. S.; Lee, Y.-J.; Choi, S. Y.; Park, Y. S.; Yoon, K. B. Self-Assembly of β-Glucosidase and D-Glucose-Tethering Zeolite Crystals Into Fibrous Aggregates. *J. Am. Chem. Soc.* **2000**, *122*, 12151–12157.

(S5) Kurzatkowska, K.; Dolusic, E.; Dehaen, W.; Sieron-Stołtny, K.; Sieron, A.; Radecka, H. Gold Electrode Incorporating Corrole as an Ion-Channel Mimetic Sensor for Determination of Dopamine. *Analytical chemistry* **2009**, *81*, 7397–7405.

(S6) Tsukruk, V. V.; Lander, L. M.; Brittain, W. J. Atomic Force Microscopy of C_{60} Tethered to a Self-Assembled Monolayer. *Langmuir* **1994**, *10*, 996–999.

(S7) Li, W.; Virtanen, J. A.; Penner, R. M. Self-Assembly of N-Alkanethiolate Monolayers on Silver Nanostructures: Determination of the Apparent Thickness of the Monolayer by Scanning Tunneling Microscopy. *The Journal of Physical Chemistry* **1994**, *98*, 11751–11755.

(S8) Itoh, Y.; Kim, B.; Gearba, R. I.; Tremblay, N. J.; Pindak, R.; Matsuo, Y.; Nakamura, E.; Nuckolls, C. Simple formation of C60 and C60-ferrocene conjugated mono-

layers anchored onto silicon oxide with five carboxylic acids and their transistor applications. *Chemistry of Materials* **2011**, *23*, 970–975.

(S9) Castañeda Ocampo, O. E.; Gordiichuk, P.; Catarci, S.; Gautier, D. A.; Herrmann, A.; Chiechi, R. C. Mechanism of Orientation-Dependent Asymmetric Charge Transport in Tunneling Junctions Comprising Photosystem I. *J. Am. Chem. Soc.* **2015**, *137*, 8419–8427.